

Programmable superconducting neuron with intrinsic in-memory computation and dual-timescale plasticity for ultra-efficient neuromorphic computing

Muen Wang, Shucheng Yang, Yuxiang Lin, Yuntian Gao, Xue Zhang, Xiaoping Gao, Minghui Niu, Huanli Liu, Yikang Wan, Wei Peng, Jie Ren*

Abstract

The escalating energy demands of artificial intelligence pose a critical challenge to conventional computing. Leveraging the efficiency of event-driven, in-memory neuromorphic architectures into the superconducting circuits with ultra-high speed and low power dissipation advantages offers a promising solution to energy-efficient computing. However, the potential of such a solution has yet to be realized, owing to the absence of a fundamental superconducting unit that unifies programmability, local memory, and multi-timescale plasticity. Here, we introduce a programmable Josephson-junction-based leaky integrate-and-fire (LIF) neuron that features intrinsic static memory and precise programmability by encoding somatic and synaptic parameters directly in the bias current. This neuron is also capable of dual-timescale plasticity: picosecond-scale short-term modulation of spike transmission and long-term weight retention exceeding 10^4 seconds, facilitating both rapid temporal adaptation and robust weight storage. It can operate up to 45 GHz with femtojoule-level energy dissipation per spike, and supports 10 somatic threshold levels and 20 synaptic states. Furthermore, we demonstrate a crossbar-based spiking neural network (SNN) utilizing this neuron, which achieves outstanding performance across multiple tasks. By fusing computation, memory and plasticity into a single superconducting unit, our work paves the way for the next generation of ultrafast, energy-efficient neuromorphic computing.

Keywords: Neuromorphic Computing, Superconducting Single-Flux-Quantum Circuits, Spiking Neural Networks

Main

The rapid growth of artificial intelligence (AI) infrastructure continues to challenge the capabilities of conventional computing architecture built on metal-oxide-semiconductor (CMOS) platforms in reducing energy consumption and latency of computation and in minimizing data movement by performing computations near memory¹. Neuromorphic computing, which is a bio-inspired energy-efficient information processing solution, has emerged as a very strong alternative for AI infrastructure by taking advantages of event-driven operation and in-memory computation². Modern CMOS neuromorphic processors have demonstrated impressive levels of parallelism and event-driven efficiency³⁻⁸, yet they remain fundamentally limited by transistor leakage, capacitive switching energy, and the memory-computation separation inherent to Von Neumann architectures. Consequently, even with event-driven architectures, the energy consumption remains in the range of 10^{-12} to 10^{-10} J per synaptic operation, which is nearly ten orders of magnitude higher than the theoretical minimum for room-temperature computing (the Landauer bound $k_B T \ln 2 \approx 2.9 \times 10^{-21}$ J at 300 K)⁹. Furthermore, CMOS circuits are typically confined to operating frequencies below a few GHz¹⁰, since scaling clock speeds further results in prohibitive power dissipation and associated thermal bottlenecks that impede effective heat extraction. As a result, achieving high compute throughput and energy-efficient AI infrastructure requires a new class of hardware that unifies the following features: ultralow energy consumption, ultrafast dynamics,

and learning capability.

Superconducting circuits, built upon Josephson junctions (JJs), features ultrafast and natural pulse-based dynamics (Fig. 1a)¹¹, giving rise to an intrinsic information processing similarity between superconducting circuits and biological neuron networks. A biological neuron can be abstracted into four functional components: dendrite, soma, axon, and synapse (Fig. 1b). Among them, the functionalities of biological axon and dendrite can easily be emulated by low-loss Josephson transmission line (JTL) that enables long-distance pulse propagation, and by splitter (SPL) and confluence buffer (CB) that fanout and merge pulses¹², respectively, as illustrated in Fig. 1b.

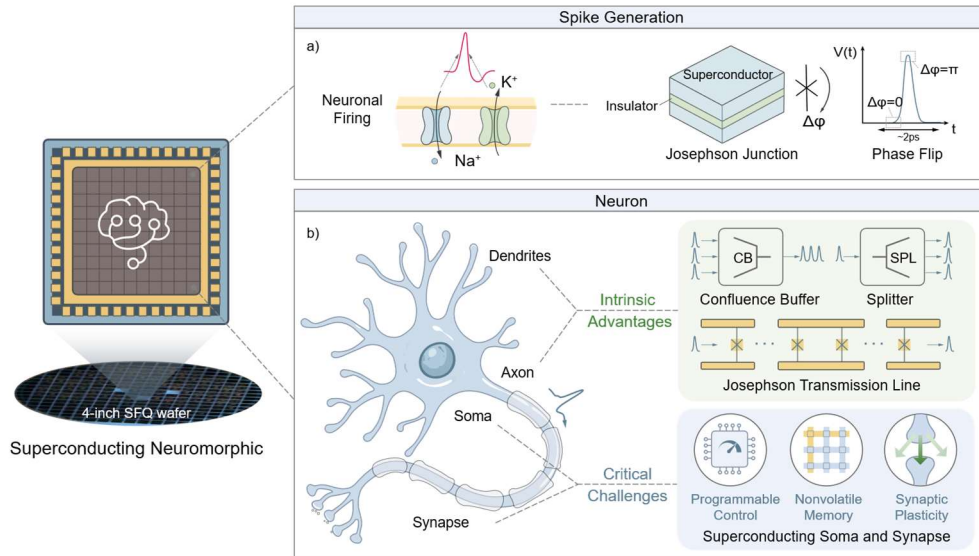


Fig. 1 | Biomimetic mapping of neuronal dynamics and morphology to superconducting single-flux-quantum circuits. **a** Comparison of the fundamental spike generation mechanisms. The biological action potential, driven by the transmembrane influx and efflux of sodium (Na^+) and potassium (K^+) ions, is analogous to the dynamics of a superconducting Josephson junction. In the superconducting domain, a SFQ voltage pulse $V(t)$ is generated via a 2π phase flip. **b** Structure and functional components of a biological neuron and their corresponding proposed superconducting circuit elements. The signal integration in dendrites and branching in axons correspond to the Confluence Buffer (CB) and Splitter (SPL) logic gates, respectively. The propagation of signals along the axon is readily realized with a proven technology, i.e., Josephson Transmission Line (JTL). Conversely, realizing the full functionalities of the soma and synapses remains a critical challenge for superconducting electronics, necessitating the development of programmable control, local memory, and synaptic plasticity mechanisms.

Recent studies on emerging neuromorphic platforms have shown that advanced neuromorphic computing requires three core circuit capabilities^{13,14}: 1) near-memory or in-memory computing capabilities for minimizing the latency and energy overheads associated with data movement, 2) fine-grained programmability for network reconfiguration, and 3) coexisting multi-timescale plasticity to support both rapid adaptation and long-term memory. Since the soma and synapse constitute the fundamental building blocks of neural networks, efficiently meeting these requirements places significant design and implementation demands on both components (Fig. 1b). Prior studies on superconducting neurons have yet to demonstrate the above comprehensive capabilities in a single neuron^{15–20}. Here we propose a practical solution, named as SPINIC (*Superconducting Programmable*

spiking Neuromorphic Integrated Circuit) by combining high-speed and low-power operation with programmability, intrinsic memory, and multi-timescale plasticity. The underlying building block of our proposed SPINIC is a programmable leaky integrate-and-fire (LIF) neuron that encodes its somatic firing threshold and synaptic weights directly into tunable bias currents of the JJs, achieving programmability without complex on-chip digital control. This mechanism also simultaneously enables in-memory computing by storing neuronal parameters in situ as persistent bias currents—a fundamental branch out from traditional superconducting logic and memory paradigms. Furthermore, leveraging the unique dynamics of Josephson-junction circuits, our synapse exhibits dual-timescale plasticity: it supports picosecond-scale (10^{-12} s) short-term modulation for rapid, adaptive learning and long-term weight changes stable over 10^4 seconds for enduring memory retention, confirming that superconducting circuits have huge advantages over conventional hardware in emulating rich neurobiological features through elegant physical design.

Superconducting Neuron: A Close Biomimetic Analogy to Biological Neurons

As illustrated in Fig. 2a, among the four functional components of a superconducting neuron, the soma and synapse involve great computational processing complexity and thus require sophisticated circuit implementations. Mizugaki et al²¹. previously introduced a two-Josephson-junction circuit resembling the topology shown in Fig. 2b. However, they implemented it exclusively as a fixed-weight synapse that was hardwired with a static resistor and therefore could not be dynamically adjusted. Here, we adopt this original synapse circuit topology but reinvented it to become a compact programmable LIF soma (Fig. 2b), wherein the firing threshold is continuously tunable via an external bias current. In our proposed soma circuit, the superconducting inductor (L) stores quantum flux and generates loop current as membrane potential, while the resistor (R) induces leakage to govern the decay time constant (τ) of the loop current. Our simulation results show that τ can be precisely tuned as $\tau \sim L/R$ (Fig. 2c). For instance, a combination of picohenry-level inductance and sub-ohm resistance leads to a τ of tens of picoseconds, enabling spike computation speed exceeding 40 GHz (See circuit details in Supplementary Fig. 1). Furthermore, our circuit exhibits reliable firing triggered by a specific threshold (defined as the number of input pulses required to elicit an output spike) and reset behaviors (e.g., Fig. 2d shows the circuit response under threshold = 5), enabling ultra-fast neuromorphic processing. This reinvented soma overcomes the limitations of original design to realize highly biomimetic LIF functionality. Crucially, it unlocks the potential for analog, multi-level programming of neuronal parameters by allowing the loop current (I_{loop}) integration and firing threshold to be modulated directly via bias currents. This bias-current-based programming methodology will be elaborated upon in the following section.

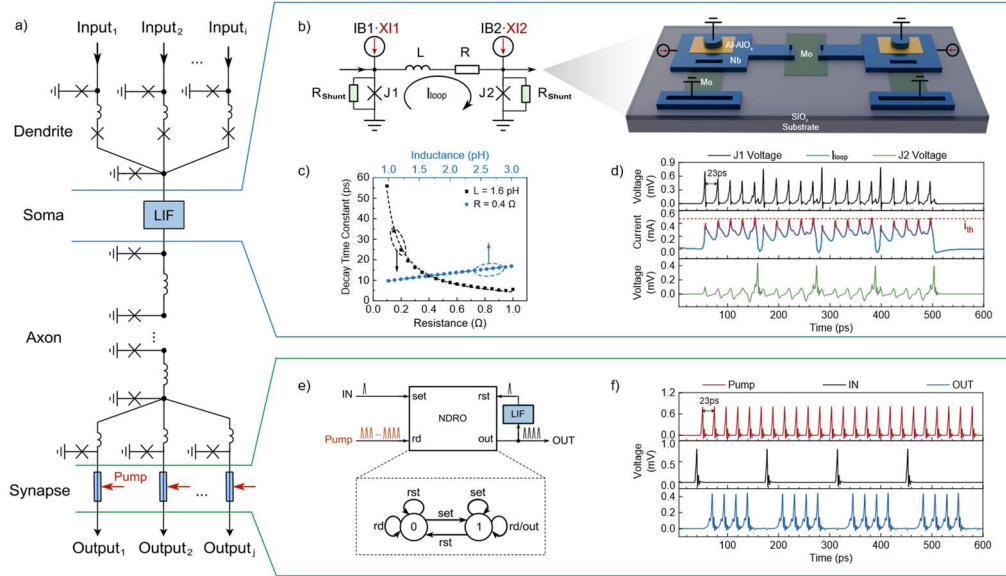


Fig. 2 | Design of the superconducting neuron. **a** Schematic of the superconducting neuron, where the dendrite and axon are implemented using CB, JTL and SPL structures. **b** Circuit and three-dimensional schematic of the superconducting LIF soma. Niobium (Nb) serves as the superconducting layer, Al/AIO_x as the insulating layer, and molybdenum (Mo) as the resistive layer. The junction is maintained under a critically damped state (Stewart–McCumber parameter $\beta_c = 1$) by shunting with a resistor to suppress underdamped oscillations, thereby enabling high-speed and reproducible RSFQ operation¹². $XI1$ and $XI2$ are scaling-factor parameters used to tune the bias currents $IB1$ and $IB2$, respectively. **c** SPICE simulation of time constant vs. resistance (bottom axis) and inductance (top axis). The dashed lines represent the analytical fits according to $\tau \sim L/R$, showing a linear dependence on L (blue) and an inverse dependence on R (black). **d** SPICE simulation waveforms of the LIF soma with a threshold of 5, showing output voltages of J_1 and J_2 , and the loop current under a train of soma input pulses with a 23 ps period. **e** Synaptic circuit diagram. The synapse is constructed from an NDRO cell, with an embedded LIF (blue region) feedback path in its reset loop (See circuit details in Supplementary Fig. 1). The state machine below illustrates how "set" and "rst" inputs toggle the output state stably between "1" and "0". **f** SPICE simulation waveforms of the synapse with a weight of 4, demonstrating the corresponding input and output waveforms. See methods for detailed simulation setup for all the simulation results.

Synapses implement weighted signal transmission by modulating the amplitude of post-synaptic potentials. An ideal superconducting synapse should scale the strength of incoming spikes to realize programmable synaptic weights. However, amplitude-based weighting is incompatible with RSFQ circuits, as JTLs (for realizing biomimetic axon) normalize pulse amplitudes to a standard SFQ. To overcome this limitation, we implement synaptic weights through pulse-count modulation: a single incoming spike triggers a programmable number of pulse replications, where the integer pulse number defines the synaptic weight. Our proposed synapse in Fig. 2e integrates the previously described LIF soma circuit (hereafter LIF) internally to generate dynamic synaptic responses. By leveraging a non-destructive read-out (NDRO) circuit driven by an inject pump input and a feedback reset signal from the LIF, the synapse performs a controlled pulse-number replication determined by the embedded LIF threshold, which corresponds to the synaptic weight w . The output spike frequency of the synapse is governed by the LIF, ensuring compatibility with ultrafast spike processing of soma. Fig. 2f shows the simulation of a synapse with weight $w = 4$, where a train of pump pulses spaced 23 ps apart replicates

each *IN* spike into four output (*OUT*) pulses. This approach bypasses the difficulty of amplitude modulation of RSFQ logic while preserving picosecond-scale spike processing speed, enabling high-speed synaptic computation within a native superconducting framework.

Superconducting In-Memory Computing Enabled by Bias-Current Programming Technology

A key requirement for scalable neuromorphic hardware is the ability to store and update computational parameters directly within the processing elements themselves. Remarkably, the superconducting neuron and synapse presented here intrinsically fulfill this requirement: the DC bias currents that govern device dynamics also serve as persistent, analog memory variables. In this fashion, neuronal thresholds and synaptic weights are stored natively, without on-chip memory or refresh circuitry. By further utilizing this kind of feature, we propose a scheme to program neuronal parameters via tuning the bias currents. By introducing scaling factors $XI1$ and $XI2$ for $IB1$ and $IB2$ respectively (Fig. 2b), the LIF circuit exhibits a variable threshold. Specifically, $XI1$ modulates the integration of the loop current from input pulses, while $XI2$ sets the firing threshold by fine-tuning the bias point of J_2 . As shown in Fig. 3a, our numerical simulation demonstrates that varying $XI1$ and $XI2$ from 0.5 to 1.5 yields ten discrete soma thresholds from 1 to 10, thereby realizing superconducting neurons with programmable states (see theoretical derivations in Supplementary). This finding is also confirmed in experiments using the soma and synapse circuits fabricated with the SIMIT-Nb03P process²² (see experimental setup in Supplementary Fig. 2). The fabricated circuit achieves also 10 distinct threshold levels, corresponding to integration thresholds from 1 to 10. The close correspondence between numerical simulations and experimental results confirms the accuracy of the LIF model implementation and demonstrates precise, reproducible control over neuronal behavior through analog bias-current programming.

For our synapse, a control parameter resolution of at least 4 bits is targeted, which is considered sufficient for low-precision spiking neural network (SNN) computations²³. To fulfill our design requirement, an additional pump bias current channel ($IB3$, with a scaling factor of $XI3$, as highlighted in red in Supplementary Fig. 1b) is added adjacent to the LIF unit. This design is validated in experiments with results demonstrating precise control of the LIF's trigger current, enabling synaptic weight outputs ranging from 1 to 20, as shown in Fig. 3b. Our results further suggest that increasing any of the three bias currents reduces the threshold for flux integration, thereby increasing the probability of trigger events and effectively decreasing the synaptic weight. The mechanism behind this continuous and analog tuning behavior arises from the fundamental phase dynamics of JJs: altering bias current reshapes the potential landscape of JJs, enabling precise and reversible control over the likelihood of SFQ pulse generation. By utilizing this mechanism, precise in situ programming of synaptic weight is achieved with minimal hardware overhead. By integrating storage and computation parameters into the same circuit, the system avoids data movement overheads and realizes an intrinsic form of computing-in-memory (CIM).

Short-Term and Long-Term Plasticity in Superconducting Synapses

The intrinsic plasticity of synapses enables artificial neurons to dynamically adjust their excitability, mimicking the adaptive abilities of biological neurons. This functionality optimizes information processing efficiency and significantly enhances learning capacity²⁴. Unlike conventional memristive synapses that typically exhibit conductance plasticity^{25–27}, our synapse achieves plasticity by modulating both the integration and the firing current within the LIF feedback loop. Long-term plasticity (LTP) is

realized via varying the bias current of JJs in the LIF feedback loop, allowing stable weight adjustment and thus supporting learning mechanisms. Fig. 3c presents simulation results for three distinct weight states over a 200 ns duration with a zoom-in view for detailed waveform. Although the simulation timespan is constrained by the high computational cost of analog transient analysis, the observed long-term stability effectively validates the circuit's dynamic robustness. Short-term plasticity (STP) arises from the temporal dynamics of loop current accumulation, where the frequency of an input pulse train directly governs the extent of current decay between spikes. As illustrated in Fig. 3d, our circuit simulation results show that altering the input pulse frequency or equivalently the pulse period, can instantly increase or decrease the decay of the loop current during the temporal interval between two consecutive input pulses, thereby adjusting the number of output synaptic pulses. Simulations with input frequencies ranging from 35 to 45 GHz (equivalent to pulse periods of 28.6–22.2 ps) reveal substantial changes in synaptic weight. This indicates that modulating the pulse period by mere picoseconds is sufficient to effectively tune the short-term excitability of the synapse.

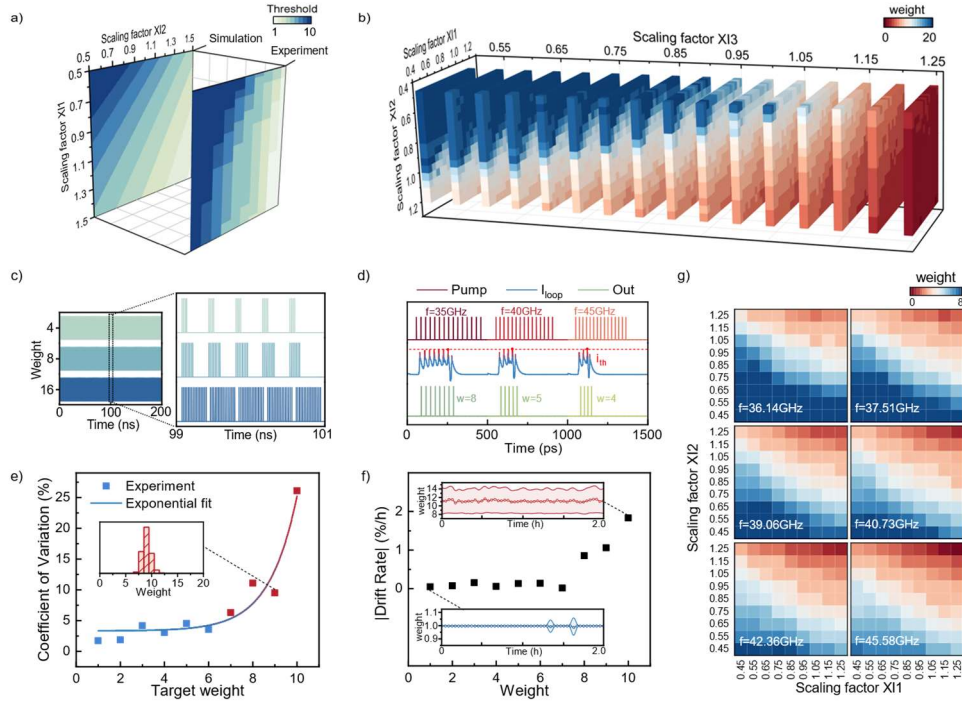


Fig. 3 | Design and experimental characterizations of our proposed superconducting neuron with programmability and dual-plasticity. **a** Numerical simulation and experimental results showing the impact of the bias current scaling factors on the soma threshold. **b** Experimental result showing the relationship between the bias current scaling factors and the synaptic weight. **c** Simulation of long-term plasticity. Multiple stable output cycles are shown over approximately 200 ns. The results with weights of 4, 8, and 16 are shown respectively, with corresponding bias-current scaling factors ($XI1$, $XI2$, $XI3$) being: (1.2, 1.2, 1.0), (1, 1, 0.8), and (0.95, 0.85, 0.55). Right part shows a zoom-in view of a representative waveforms during the 99–101 ns interval. During simulation, the pump signal is applied continuously. To enable sustained synaptic output, input signals are re-injected via the IN terminal (see Fig. 2e) following each internal reset event. **d** Simulation of short-term plasticity. As the input pulse frequency increases from 35GHz to 40GHz and then to 45GHz, the synaptic weight decreases from 8 to 5 and then to 4. **e** Coefficient of variation (CV) of synaptic weights. Square symbols represent the measured CV across different target weights, fitted with an exponential curve. The inset displays the distribution of experimental results for a target

weight of $w=9$. **f** Drift rates (DR) of synaptic weights. Black squares denote the absolute DR values for ten target weights. The insets illustrate the temporal evolution of weights for the most ($w=1$) and least ($w=10$) stable cases. Solid lines and error bands correspond to the mean and standard deviation, respectively, calculated over 200-cycle bins. **g** STP characteristics of the synapse. The heatmap illustrates the dependence of synaptic weight on $XI1$ and $XI2$ at six frequency points from 36.14 GHz to 45.58 GHz. For clarity, $XI3$ is fixed at 1.0 here.

To investigate LTP of our synapse experimentally, we recorded weight states encoded by bias currents over a continuous 20-hour period. Ten distinct weight states were each evaluated over 10,000 high-frequency hardware test cycles. The extracted coefficient of variation (CV) and drift rate (DR), shown in Fig. 3e and Fig. 3f, are then used to quantify the stability. The results indicate that CV increases with the target weight state, exhibiting an approximately exponential trend. This behavior arises from the fact that the accumulation of input pulses diminishes the margins between adjacent loop-current peaks (Supplementary Fig. 3), resulting in an exponential reduction in current resolution. Based on a standard 5% CV tolerance for typical neuromorphic systems^{28,29}, we achieve six distinguishable stable states (i.e., $w \leq 6$). Notably, all ten weights exhibit negligible temporal drift ($|DR| < 2\%$), confirming the stability of the programming currents and the robustness of our implemented circuits³⁰. STP was characterized by measuring synaptic weight responses to different input pulse frequencies. Fig. 3g shows the relationship between input frequency (36.14 - 45.58 GHz) and synaptic weight at six representative frequency points (See Methods for high-frequency calibration). Increasing the input frequency reduces the synaptic weight, consistent with our previous analysis. The average weight reduction is approximately 0.22 per GHz, demonstrating frequency-modulated STP behavior. By unifying rapid synaptic modulation and long-term weight storage within a single superconducting circuit, our architecture achieves multi-timescale learning with minimal hardware overhead and near-zero dynamic power. The realization of dual-plasticity enables building brain-inspired processors on a high-energy-efficient superconducting platform to achieve scalable bio-inspired learning, with short-term response speeds surpassing the performance limits of CMOS or emerging resistive devices, while maintaining excellent long-term retention capabilities.

Network Architecture Design and a Small-Scale Experimental Validation

To evaluate system-level behavior of our proposed superconducting neuron in SNN, we implemented a superconducting neuromorphic architecture called SPINIC, as mentioned above. Specifically, we fabricated and characterized a SPINIC prototype core with the array scale of 4×4 to demonstrate its scalable processing capabilities. As shown in Fig. 4a, the network circuitry (1,050 JJs) occupies approximately one-third of the total circuit area, while the remaining area is dedicated to auxiliary high-speed test structures (2,474 JJs). This architecture employs a crossbar structure (Supplementary Fig. 4) in which all parameters—somatic thresholds and synaptic weights—are set through static DC bias currents applied to the corresponding JJs. This eliminates the need for any peripheral digital memory or weight-loading circuitry. Once programmed, all network states remain static under constant bias, with no refresh overhead.

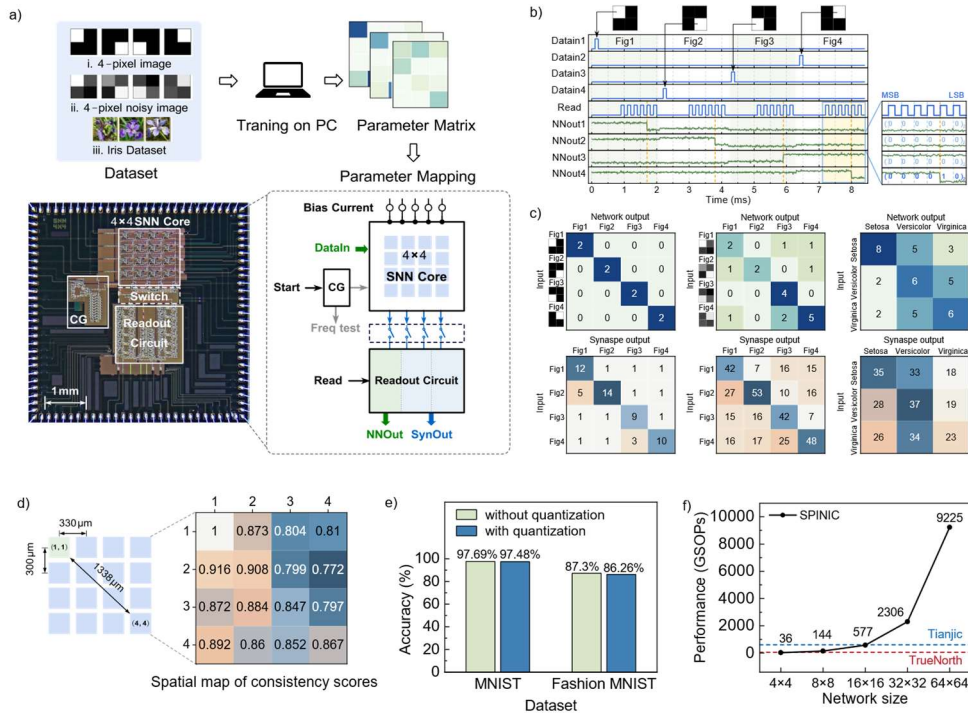


Fig. 4 | Experimental results of the 4×4 SPINIC core. **a** Testing workflow, chip micrograph, and circuit schematic of the 4×4 SPINIC. The blue diagram illustrates the three datasets used for testing. After training is completed on a PC, the resulting network parameters are mapped to the SPINIC core via bias currents to perform hardware-accelerated inference. The chip contains four major modules: a high-frequency clock generator, the SNN core, column selection switches, and counting/readout units. **b** Example of measured waveforms from the 4×4 SPINIC. Blue traces represent input signals, where rising edges of external voltage levels are converted into pulses by an on-chip digital-to-SFQ (D2Q) converter. Green traces correspond to output signals, which are reconverted into voltage levels by an on-chip SFQ-to-digital (Q2D) converter, with each edge representing an output spike. Binary counting results of the network are determined by correlating each "NNout" signal with the "readout" signal, as shown in the zoom-in view. **c** Inference results for the three datasets. From left to right: outcomes for datasets i–iii shown in Fig. 4a. Top row represents network outputs, while bottom row shows synaptic-layer activities. **d** Spatial consistency validation of synaptic parameters in SPINIC. The left panel shows the spatial distribution of the 16 synapses in the network. Reference against to the synapse at the green-labeled position (1,1), the remaining 15 synapses have their consistency score displayed in the heatmap on the right. **e** Algorithmic accuracy of SPINIC on MNIST and Fashion-MNIST. Bar charts show the comparison between the full-precision baseline and quantized networks under hardware-precision constraints, indicating very little accuracy degradation due to quantization. **f** Throughput of SPINIC at different network scales and comparison against CMOS-based benchmarks, i.e., TrueNorth and Tianjic.

In our experiments, we constructed several representative neural networks to verify the programmability of the circuits. Test datasets, including 4-pixel images, 4-pixel noisy images, and the Iris dataset (Fig. 4a), were first used to train each network offline, thereby determining the corresponding synaptic weight matrices and somatic firing thresholds, which were subsequently mapped to the hardware by adjusting the corresponding bias currents. To ensure accurate parameter mapping, we established a calibration relationship between the bias currents and the neuronal parameters prior to functional network testing. This was accomplished by sweeping the current scaling factors to directly measure the resulting thresholds and weights, producing a deterministic current-to-parameter lookup table for accurate

programming later on. The reconfiguration time of the entire 4×4 network is only on the order of microseconds, which in our case is dictated by the limited update rate of our external DC bias sources³¹ (a limit that in principle could be further reduced with on-circuitry bias sources), demonstrating true general-purpose programmability. Fig. 4b displays representative measured waveforms from a 4-pixel image inference test, showing input spikes (DataIn1–4), readout signals (Read), and output pulses (NNout1–4). Complete results across all three test sets are summarized in Fig. 4c, demonstrating full consistency with both algorithmic expectations and circuit simulations. Overall, the 4×4 SPINIC core successfully performed accurate classification on these representative datasets, confirming the feasibility and programmability of our proposed superconducting neuromorphic architecture and laying a foundation for scaling toward larger systems.

Crucially, parameter variations induced by fabrication inhomogeneity can lead to unintended weight deviations, thereby degrading the computing accuracy of the network. Therefore, verifying the consistency across spatial scales is a prerequisite for ensuring the robustness of large-scale superconducting neuromorphic systems. Therefore, to evaluate the spatial consistency of the proposed superconducting neurons, we experimentally examined the distribution of a key parameter, i.e., weight values, of the 16 synapses within the network. As shown in Fig. 4d, the on-chip distance between synaptic circuits ranges from 300 μm to 1338 μm . The weight values were extracted through bias current scanning, and a two-sample Kolmogorov–Smirnov (K-S) test was performed for statistical analysis³² (see details in Supplementary). The synapse located at position (1,1) was used as a reference to evaluate the other 15 synapses. All other synapses exhibited very small K-S distances ($D < 0.15$) and nearly overlapping empirical cumulative distribution functions (ECDFs) with the reference, indicating high consistency in weight distribution across the chip. This suggests excellent spatial robustness of the synaptic circuit implementation.

System-level performance and scalability

To evaluate the computational prospect of the SPINIC architecture under hardware-intrinsic constraints, we benchmarked its inference capabilities using standard neuromorphic datasets (MNIST³³ and Fashion-MNIST³⁴). A four-layer SNN model was designed, consisting of an input flattening (IF) layer and three fully connected (FC) layers with dimensions of IF(28 \times 28)-FC(512)-FC(64)-FC(10). Given that superconducting logic inherently operates with limited parameter precision (for instance, 20 discrete weight states in our system), we rigorously evaluated the impact of the quantization effect on the network performance. As illustrated in Fig. 4e, this architecture exhibits remarkable robustness to reduced-precision constraints. Compared to full-precision baselines, the quantized SPINIC model incurs a marginal accuracy loss of only 0.21% for MNIST and 1.04% for Fashion-MNIST. This validates that the bias-current programming method in our proposed superconducting neuromorphic scheme effectively supports accurate inference despite the limited parameter bit-width of neurons.

The fundamental advantage of the SPINIC paradigm lies in its energetic regime. In superconducting SFQ circuits, total power consumption consists of static and dynamic components³⁵. Based on the measured device characteristics of SPINIC, the energy consumption for a single synaptic operation here is only 3.21 fJ/SOP. This femtojoule-level operation represents a reduction of approximately three orders of magnitude compared to state-of-the-art CMOS neuromorphic platforms (Table 1). We further project the system-level scalability of SPINIC by extending our experimentally characterized 4×4 core to larger integration scales (refer to Supplementary for detailed calculation). While current superconducting fabrication processes have demonstrated circuits with up to 1.03×10^6 JJs³⁶, practical integration is often

constrained by flux trapping and bias distribution overheads. Under a conservative estimation of an integration scale of less than 10^6 JJs, a medium-scale 32×32 SPINIC core (requiring $\sim 67,500$ JJs) should be feasible with a total power consumption of roughly only 24.75 mW. In order to quantify its compute throughput, the metric of synaptic operations per second (SOPS), first introduced by IBM³⁷, is used. As illustrated in Fig. 4f, we evaluated the peak performance of SPINIC cores ranging from 4×4 to 64×64 in size and compared that with advanced CMOS-based designs. Noticeably, the 32×32 SPINIC core is capable of a peak throughput of 2,306 GSOPS, surpassing that of large-scale CMOS neuromorphic processors. Due to the ultralow switching energy and minimal delay of SFQ circuits, our SPINIC core could achieve 93,184 GSOPS/W (excluding cooling power consumption), an energy efficiency performance level at least 144 times better than the CMOS counterparts. Compared with the recently proposed superconducting SUSHI chip with similar JJ counts¹⁹, SPINIC is 10 times better in energy efficiency, attributed to its simplified and highly optimized neuron architecture. In practice, a fair comparison should take into account the cryogenic cooling power penalty of our system. Even considering an exaggerated cooling power factor of 300 times, our system is still capable of 311 GSOPS/W. With further optimization by adopting energy-efficient RSFQ (ERSFQ) technology³⁵, the static power dissipation that dominates in current designs can be virtually eliminating. The resulted system efficiency is projected to reach 8,962 GSOPS/W, a 19-fold advantage over advanced CMOS implementations.

Table 1 | Performance comparison between the SPINIC and previously reported neuromorphic hardware

	Year	Implementation	Synaptic width	GSOPS	J/SOP	GSOPs/W	
						Wo.C.※	W.C.†
SpiNNaker ³	2013	Soft-core-based	-	0.064	11.3 n	0.064	0.047
TrueNorth ⁴	2015	ASIC	1 bit	58	26 p	400	292
Loihi ⁵	2018	ASIC	1 to 9 bit	-	23.6 p	42	31
Tianjic ⁶	2020	ASIC	8 bit	608	1.54 p	649	474
Spiker ⁷	2022	FPGA-based	16 bit	-	41 n	0.024	0.018
Darwin ⁸	2024	ASIC	1/2/4/8/16 bit	-	5.47 p	183	134
SUSHI ¹⁹	2023	Superconducting Devices	1 bit	1355	-	32,336 ★	108 ★
SPINIC	2026	Superconducting Devices	4 to 5 bit	2,306	3.21 f	93,184 314,000 ★	311 1046 ★
						2,693,949 ▲	8,962 ▲

※ Without cooling cost. † Cooling overhead is estimated at $1.37 \times$ for CMOS chips (global data center average in 2020)³⁸ and intentionally exaggerated to $300 \times$ for superconducting chips to highlight performance under highly unfavorable cooling assumptions.

★ The estimation does not include the layout and interconnect overhead required for practical superconducting implementation.

▲ Based on the ERSFQ technology.

Conclusion

We have demonstrated a fully programmable, scalable superconducting neuromorphic architecture that unifies the extreme speed of RSFQ logic with the adaptability required for intelligent processing. By identifying bias currents as a new degree of freedom for parameter encoding, SPINIC overcomes the long-standing challenge of implementing local memory in standard superconducting circuits. This innovation enables the construction of neurons that are not only orders of magnitude faster and more efficient than their semiconductor counterparts but also capable of complex, multi-timescale learning. As the AI computational infrastructure starts to approach the power wall, SPINIC offers a practical, scalable alternative, paving the way for a new generation of hyper-efficient cognitive hardware that operates at an ultra-fast speed and with energy efficiency a huge step close to the physical limit.

Methods

Fabrication process of SPINIC

The SPINIC chip and the neuron circuits were fabricated using the SIMIT-Nb03P superconducting integration process. This process employs 4-inch surface-oxidized silicon wafers as the substrate, with high-quality SiO₂, deposited by plasma-enhanced chemical vapor deposition (PECVD), serving as the insulation layer, Ti/Au acting as the contact layer, and Nb superconducting layer prepared by magnetron sputtering. Highly stable and reproducible Josephson junctions were achieved by depositing Nb/Al–AlO_x/Nb trilayer films without breaking the vacuum, followed by junction definition via deep ultraviolet (DUV) stepper lithography and inductively coupled plasma (ICP) etching.

Experimental setups for superconducting circuits

The processed 4-inch wafer was first diced into 5×5 mm² chips, which were then wire-bonded to a printed circuit board (PCB) using highly conductive aluminum wires to minimize electrical losses. The PCB was mounted into a 116-channel cryogenic probe, with electrical connections established between the board and the probe electrodes. The probe was immersed in a liquid helium dewar, cooling the chip to an operating temperature of 4.2 K. Electrical characterization was performed via three DB50 cables connecting the probe to an OCTOPUX-4FH/128H³⁹ multi-channel automated test system—a versatile low-frequency measurement platform comprising 128 high-precision DAC and ADC channels, along with a digital voltmeter (DVM) offering 1 μV resolution. System control and circuit testing were automated using a custom MATLAB script to coordinate all OCTOPUX channels.

On-chip high-frequency testing method

The on-chip clock generator (CG) frequency was adjusted via changing its bias current. Higher bias currents accelerate junction switching and reduce pulse transmission delay, thus increasing the CG frequency. The actual CG frequency was determined from the average voltage across the JJs using Faraday's law. When SFQ pulses pass a junction at frequency f , the junction voltage satisfies $V = f\Phi_0$, where Φ_0 is the superconducting flux quantum. Therefore, by measuring the average voltage $\overline{V_{CG}}$, the CG frequency can be determined using the following formula,

$$f = \frac{\overline{V_{CG}}}{\Phi_0}$$

Notice, the average voltage across the junction is measured using the above mentioned high-precision DVM of the OCTOPUX system.

SPICE Simulation Setup

All circuit-level simulations were performed using in-house developed JSICsim⁴⁰, a SPICE-compatible simulator tailored for superconducting integrated circuits. The structural netlist was generated from the schematic of the neuron unit and its testbench, preserving the hierarchical connectivity of the physical design. To capture the dynamic switching behavior of JJs, we specified timing and triggering conditions using SFQ Hardware Description Language (SFQ HDL). This behavioral description was co-exported with the netlist and translated into Verilog-A models compatible with JSICsim as needed, enabling mixed structural-behavioral transient simulations.

Functional correctness was first verified under nominal process conditions. Subsequently, we quantified circuit robustness through operating margin extraction. Specifically, we employed a bisection-based search algorithm to determine the tolerance limits of three key process parameters: the bias current scaling factor (XI), Josephson critical current density scaling factor (XJ), and inductance scaling factor (XL). For each parameter, the algorithm iteratively narrowed the interval between a known functional point and a failure point until the boundary of correct SFQ pulse propagation was identified within a predefined resolution. This approach efficiently maps the process window, in which the circuit remains operational despite fabrication-induced variations.

Reference

1. S, H., Bhat, N. & Goswami, S. Neuromorphic pathways for transforming AI hardware. *Nat Electron* **8**, 752–756 (2025).
2. Mead, C. Neuromorphic electronic systems. *Proceedings of the IEEE* **78**, 1629–1636 (1990).
3. Furber, S. B., Galluppi, F., Temple, S. & Plana, L. A. The SpiNNaker Project. *Proceedings of the IEEE* **102**, 652–665 (2014).
4. Merolla, P. A. *et al.* A million spiking-neuron integrated circuit with a scalable communication network and interface. *Science* **345**, 668–673 (2014).
5. Davies, M. *et al.* Loihi: A Neuromorphic Manycore Processor with On-Chip Learning. *IEEE Micro* **38**, 82–99 (2018).
6. Pei, J. *et al.* Towards artificial general intelligence with hybrid Tianjic chip architecture. *Nature* **572**, 106–111 (2019).
7. Carpegna, A., Savino, A. & Di Carlo, S. Spiker: an FPGA-optimized Hardware accelerator for Spiking Neural Networks. in *2022 IEEE Computer Society Annual Symposium on VLSI (ISVLSI)* 14–19 (2022). doi:10.1109/ISVLSI54635.2022.00016.
8. Ma, D. *et al.* Darwin3: a large-scale neuromorphic chip with a novel ISA and on-chip learning. *NSR* **11**, nwae102 (2024).
9. Bérut, A. *et al.* Experimental verification of Landauer’s principle linking information and thermodynamics. *Nature* **483**, 187–189 (2012).
10. Horowitz, M. 1.1 Computing’s energy problem (and what we can do about it). in *2014 IEEE International Solid-State Circuits Conference Digest of Technical Papers (ISSCC)* 10–14 (2014). doi:10.1109/ISSCC.2014.6757323.
11. Schneider, M. *et al.* SuperMind: a survey of the potential of superconducting electronics for neuromorphic computing. *Supercond. Sci. Technol.* **35**, 053001 (2022).
12. Likharev, K. K. & Semenov, V. K. RSFQ logic/memory family: a new Josephson-junction technology for sub-terahertz-clock-frequency digital systems. *IEEE Transactions on Applied*

Superconductivity **1**, 3–28 (1991).

13. Cao, T. *et al.* Emerging memory devices for neuromorphic computing in the Internet of Medical Things. *CR-PHYS-SC* **6**, (2025).
14. Muir, D. R. & Sheik, S. The road to commercial success for neuromorphic technologies. *Nat Commun* **16**, 3586 (2025).
15. Zhang, H., Gang, C., Xu, C., Gong, G. & Lu, H. Brain-Inspired Spiking Neural Network Using Superconducting Devices. *IEEE Transactions on Emerging Topics in Computational Intelligence* **7**, 271–277 (2023).
16. Dayton, I. M. *et al.* Experimental Demonstration of a Josephson Magnetic Memory Cell With a Programmable π -Junction. *IEEE Magnetics Letters* **9**, 1–5 (2018).
17. Segall, K., Nichols, L., Friend, W. & Kaplan, S. B. Learning dynamics on the picosecond timescale in a superconducting synapse structure. Preprint at <https://doi.org/10.48550/arXiv.2504.02754> (2025).
18. Golden, E. B., Semenov, V. K. & Tolpygo, S. K. Development of a Neuromorphic Network Using BioSFQ Circuits. *IEEE Transactions on Applied Superconductivity* **35**, 1–7 (2025).
19. Liu, Z. *et al.* SUSHI: Ultra-High-Speed and Ultra-Low-Power Neuromorphic Chip Using Superconducting Single-Flux-Quantum Circuits. in *56th Annual IEEE/ACM International Symposium on Microarchitecture* 614–627 (ACM, Toronto ON Canada, 2023). doi:10.1145/3613424.3623787.
20. Song, C. *et al.* SuperSNN: A Hardware-Aware Framework for Physically Realizable, High-Performance Superconducting Spiking Neural Network Chips. Preprint at <https://doi.org/10.48550/arXiv.2509.05532> (2025).
21. Mizugaki, Y., Nakajima, K., Sawada, Y. & Yamashita, T. Superconducting neural circuits using fluxon pulses. *Appl. Phys. Lett.* **62**, 762–764 (1993).
22. Ying, L. *et al.* Development of Multi-Layer Fabrication Process for SFQ Large Scale Integrated Digital Circuits. *IEEE Transactions on Applied Superconductivity* **31**, 1–4 (2021).
23. Pfeil, T. *et al.* Is a 4-Bit Synaptic Weight Resolution Enough? – Constraints on Enabling Spike-Timing Dependent Plasticity in Neuromorphic Hardware. *Front. Neurosci.* **6**, (2012).
24. George, R. *et al.* Plasticity and Adaptation in Neuromorphic Biohybrid Systems. *iScience* **23**, 101589 (2020).
25. Berdan, R. *et al.* Emulating short-term synaptic dynamics with memristive devices. *Sci Rep* **6**, 18639 (2016).
26. Boybat, I. *et al.* Neuromorphic computing with multi-memristive synapses. *Nat Commun* **9**, 2514 (2018).
27. Huang, W. *et al.* Memristive Artificial Synapses for Neuromorphic Computing. *Nano-Micro Lett.* **13**, 85 (2021).
28. Choi, S., Bezugam, S. S., Bhattacharya, T., Kwon, D. & Strukov, D. B. Wafer-scale fabrication of memristive passive crossbar circuits for brain-scale neuromorphic computing. *Nat Commun* **16**, 8757 (2025).
29. Hong, H. *et al.* Memristor-based adaptive analog-to-digital conversion for efficient and accurate compute-in-memory. *Nat Commun* **16**, 9749 (2025).
30. Stathopoulos, S., Michalas, L., Khiat, A., Serb, A. & Prodromakis, T. An Electrical Characterisation Methodology for Benchmarking Memristive Device Technologies. *Sci Rep* **9**, 19412 (2019).
31. Zinoviev, D. Y. & Polyakov, Y. A. Octopus: an advanced automated setup for testing superconductor circuits. *IEEE Transactions on Applied Superconductivity* **7**, 3240–3243 (1997).
32. Massey Jr., F. J. The Kolmogorov-Smirnov Test for Goodness of Fit. *Journal of the American*

Statistical Association **46**, 68–78 (1951).

33. Lecun, Y., Bottou, L., Bengio, Y. & Haffner, P. Gradient-based learning applied to document recognition. *Proceedings of the IEEE* **86**, 2278–2324 (1998).

34. Xiao, H., Rasul, K. & Vollgraf, R. Fashion-MNIST: a Novel Image Dataset for Benchmarking Machine Learning Algorithms. Preprint at <https://doi.org/10.48550/arXiv.1708.07747> (2017).

35. Mukhanov, O. A. Energy-Efficient Single Flux Quantum Technology. *IEEE Transactions on Applied Superconductivity* **21**, 760–769 (2011).

36. IRDS™ 2023: Cryogenic Electronics and Quantum Information Processing - IEEE IRDS™. <https://irds.ieee.org/editions/2023/20-roadmap-2023-edition/129-irds%E2%84%A2-2023-cryogenic-electronics-and-quantum-information-processing>.

37. Akopyan, F. *et al.* TrueNorth: Design and Tool Flow of a 65 mW 1 Million Neuron Programmable Neurosynaptic Chip. *IEEE Transactions on Computer-Aided Design of Integrated Circuits and Systems* **34**, 1537–1557 (2015).

38. Isazadeh, A., Ziviani, D. & Claridge, D. E. Global trends, performance metrics, and energy reduction measures in datacom facilities. *Renewable and Sustainable Energy Reviews* **174**, 113149 (2023).

39. OCTOPUX - automated setup for testing superconductor circuits. redhitech.com/octopux.html. <https://www.redhitech.com/octopux.html>.

40. Yang, S., Ren, J., Liu, B. & Gao, X. JSICsim—An Analog Simulator for Superconductor Integrated Circuit. *IEEE Transactions on Circuits and Systems II: Express Briefs* **70**, 1129–1133 (2023).

Acknowledgements

The author would like to thank the SIMIT Superconducting Electronics Facility (SELF) for providing access to its state-of-the-art superconducting integrated circuit fabrication platform, and also gratefully acknowledge other members of the SFQ research group for their valuable contributions to circuit design, testing, and fabrication. This work was supported by the National Natural Science Foundation of China under Grant No. 62571520, the Autonomous deployment project of State Key Laboratory of Materials for Integrated Circuits No. SKLJC-Z2024-A03.

Author contributions

J.R. initiated and supervised the project. M.W. conceived and designed the neuron circuit and the SPINIC chip, and led the experimental characterization work, and S.Y. led the overall hardware & software co-design and system architecture planning. Y.L. developed the neural network training toolkit, and Y.G. built the superconducting measurement infrastructure. X.G. contributed to the design of additional superconducting circuits and functional units. X.Z. fabricated the superconducting integrated circuits. M.N. and H.L. established and maintained the cryogenic testing platform. M.W., S.Y., Y.W., and J.R. wrote the manuscript, with input from all authors. All authors discussed the results, contributed to data analysis, and reviewed the manuscript. M.W. and S.Y. contributed equally to this work. The study was carried out under the leadership of J.R.